Earth and Planetary Science Letters 437 (2016) 114–126

Contents lists available at ScienceDirect

Earth and Planetary Science Letters

www.elsevier.com/locate/epsl

Coupled dynamics of Earth's geomagnetic westward drift and inner core super-rotation

Guillaume Pichon *, Julien Aubert, Alexandre Fournier

Institut de Physique du Globe de Paris, Sorbonne Paris Cité, Université Paris-Diderot, UMR 7154 CNRS, 1 rue Jussieu, F-75005 Paris, France

ARTICLE INFO

Article history:
Received 4 August 2015
Received in revised form 17 November 2015
Accepted 4 January 2016
Available online xxxx
Editor: B. Buffett

Keywords:
dynamo: theories and simulations
core, outer core and inner core
core–mantle coupling
geomagnetic westward drift
inner core super-rotation

ABSTRACT

The geomagnetic westward drift and the inner core differential rotation relative to the mantle are two components of the Earth's core rotational dynamics. We present a systematic study of their long-term relationship in convective numerical simulations of the geodynamo. All models comprise gravitational coupling between the inner core and the mantle, in addition to electromagnetic coupling at the inner core and core–mantle boundaries. We show that the strength of these couplings has no influence on the global shear available in the fluid shell, the amount of which is entirely governed by the vigor of convection. This shear is distributed between the long-term westward drift and the long-term differential rotation of the inner core, in proportions controlled by the relative magnitudes of the electromagnetic and gravitational couplings. A present-day estimate of this available shear predicts a magnitude of the westward drift close to that observed on average during the last 400 yrs, which then implies a non-existent long-term inner core differential rotation. Assuming a lower mantle conductance of order 10^8 S, this in turn sets a constraint on the minimum stiffness of the inner core, the viscosity of which should be larger than 2×10^{17} Pa s for the westward drift to dominate.

1. Introduction

The geomagnetic westward drift and the inner core super-rotation are two apparently distinct signatures of rotational dynamics in the Earth's core. The understanding of their behavior is of interest to several disciplines: geomagnetism, seismology, geodynamics and geodesy. However, their possible relationship has so far received little attention.

One of the striking results of the pioneering geodynamo simulation of Glatzmaier and Roberts (1996) was the observation of a differential rotation of the inner core respectively to the mantle of about 2° per year. This was obtained by taking into account the electromagnetic coupling between the electrically conducting fluid outer core and solid inner core. Since the inner core is electrically conducting, it can indeed be permeated by a toroidal magnetic field which creates an axial electromagnetic torque (Gubbins, 1981). This generally promotes co-rotation between the inner core and the overlying fluid in the outer core, but local induction effects at the inner core boundary (ICB) allow for a residual angular velocity jump (Aurnou et al., 1996), with the angular velocity difference at the ICB opposing the shear in the outer core. The situation is hence similar to that occurring in an asynchronous motor.

Initial numerical reports of the inner core differential rotation (Glatzmaier and Roberts, 1996) gave rise to numerous seismological studies. Using differential travel-time between PKP(BC) and PKP(DF) waves, Song and Richards (1996) inferred a rotation rate of the inner core of $1.1 \pm 0.7°$ yr^{-1} in the eastward direction. Since then, many authors have revised downwards the initial estimates to a maximum rotation rate of about 0.3° yr^{-1}, for instance by using temporal variations in seismic waves travel-time (Creager, 1997; Song, 2000). Using normal modes, Laske and Masters (1999) concluded there was an absence of inner core super-rotation, and this is the accepted scenario at the present time (see Souriau and Calvet, 2015, for a review). Therefore, the seismologically inferred super-rotation may correspond to decadal fluctuations (Tkalčić et al., 2013) around an average zero differential rotation, as initially suggested by Song and Poupinet (2007).

The geomagnetic westward drift is, in contrast, much better constrained. It was first described by Halley (1692), as a westward drift of agonic lines of the Earth's magnetic field over time. It is nowadays well imaged over the last four centuries in models accounting for data acquired by mariners, observatories and satellites, as the westward drift of magnetic flux patches at the core surface (Jackson et al., 2000; Finlay and Jackson, 2003). Concentrated at the equator in the Atlantic hemisphere, these patches

* Corresponding author.
E-mail address: pichon@ipgp.fr (G. Pichon).

http://dx.doi.org/10.1016/j.epsl.2016.01.004
0012-821X/

have an average longitudinal velocity of 17 km per year over the epochs investigated by Finlay and Jackson (2003), which corresponds to an angular velocity of 0.28° yr^{-1}.

Since Roberts and Scott (1965), it is admitted that this secular variation pattern reflects advection by an underlying azimuthal flow below the core–mantle boundary (CMB). At this point, it is thus natural to imagine that the westward drift and the inner core super-rotation are the top and bottom signatures of a global radial shear in azimuthal velocities. The dynamic origin of such a global shear may reside in core polar vortices. These vortices result from the interaction between convective upwellings and Coriolis forces inside the tangent cylinder (the imaginary cylinder aligned with the rotation axis and circumscribing the inner core). They are cyclonic close to the ICB and anti-cyclonic when approaching the CMB. These polar vortices are ubiquitous features in numerical geodynamo simulations (e.g. Aubert, 2005; Sreenivasan and Jones, 2006), and appear to be in agreement with flows estimated from the geomagnetic secular variation (Olson and Aurnou, 1999), though they should be interpreted with caution as they are poorly resolved in polar regions (Eymin and Hulot, 2005). Polar vortices can provide the shear that links the inner core rotation and the westward drift, but the absolute velocities of these quantities in the frame rotating with the Earth are ultimately determined by the state of coupling between the inner core, the outer core and the mantle (Dumberry, 2007; Aubert et al., 2013).

The key ingredient here is the possibility of a gravitational torque, coupling the inner core and the mantle (Buffett, 1996). The mechanism involves density anomalies in the mantle (see Davies et al., 2014 for recent estimates) which deform the equipotential gravity surfaces by about a hundred meters close to the ICB (Buffett, 1997). The shape of the inner core adjusts to the gravity equipotential, in which case a slight misalignment between the mantle and the inner core results in a strong restoring force. If the inner core is allowed to viscously deform, though, then a super-rotation is still worth considering while creating a moderate restoring force (Buffett, 1997). A second crucial component is the coupling between the outer core and the mantle at the CMB. A primary candidate for a such coupling is again electromagnetic forces (Buffett, 1992; Holme, 1998; Buffett and Christensen, 2007). The basic idea is that there is an electrically conducting layer on the mantle side of the CMB, which again can be permeated by toroidal magnetic fields and hence can experience an electromagnetic torque (Rochester, 1960, 1962). Evidence for the existence of this layer can be obtained by looking at the out-of-phase component of the forced nutations of the Earth (Buffett, 1992; Buffett et al., 2002), which constrains the conductance of this layer to be at least 10^8S. This is supported by recent mineral physics experiments, inferring a thick post-perovskite layer (Murakami et al., 2004) of quite high conductivity (Ohta et al., 2008) or a thin layer of metallic FeO with a conductivity close to that of the core (Ohta et al., 2012).

From this discussion, it becomes obvious that the rotational state of the core is the result of a complex combination of physical effects. For example, the angular velocity jump at the ICB will be influenced by the strength of the gravitational torque exerted on the inner core and the amount of westward drift will crucially be determined by the amplitude of electromagnetic coupling at the CMB. We can however anticipate that the global amount of shear available in the outer core will be insensitive to both effects described above, as it should only be dictated by the strength of convection (Aubert, 2005). It thus appears timely to elaborate numerical geodynamo models encompassing all these effects and derive the scaling laws governing the long-term rotation components of Earth's coupled core–mantle system. From a practical standpoint, this is an incremental study adding the CMB electromagnetic coupling to the coupled Earth dynamo system which neglected its impact (Aubert et al., 2013). From a theoretical point of view, we rely on the theory developed by Dumberry (2007) in order to derive the scaling laws. We frame our analysis within the thermal wind theory (Aurnou et al., 2003; Aubert, 2005) to explain the geomagnetic westward drift. This theory is able to reproduce several observations of the Earth's magnetic field and its secular variation, such as the equatorial field patch trains of normal polarity, their wave like patterns and their inferred underlying core flows, all within a self-consistent convective model (see e.g. Aubert et al., 2013). There are alternative theories to explain the geomagnetic westward drift: magnetic winds (Livermore et al., 2013), magnetic Rossby waves (Hori et al., 2015) and mantle control (Christensen and Olson, 2003); however, these have yet to give birth to dynamical models capable of generating spontaneously the salient features of the geomagnetic secular variation we just recalled. We also restrict our analysis to electromagnetic and gravitational torques only, and do not consider other sources of coupling between the mantle and the core, such as the topographic torque, which remains poorly constrained (Roberts and Aurnou, 2012). The key geophysical questions we have in mind are the following ones: are the inner core super-rotation and the westward drift long-term features of the geodynamo? What is the physical link between these two components of the rotational dynamics of the Earth? Under what conditions does the coupled Earth dynamo model match the observed westward drift? To address these questions, we dedicate the second section to the description of our physical model, its numerical implementation, and a theoretical analysis of its long-term rotational state. That theory is successfully tested against the outputs of numerical simulations in section 3, and its geophysical implications are finally discussed in section 4.

2. Model

2.1. Conservation laws

We consider the flow of an electrically conducting, incompressible fluid of density ρ and viscosity ν, driven by convection in a spherical shell of thickness $D = r_o - r_i$, where r_i is the inner core radius and r_o is the core–mantle boundary radius. A set of spherical coordinates is chosen as (r, θ, φ), with associate unit vectors $(\mathbf{e}_r, \mathbf{e}_\theta, \mathbf{e}_\varphi)$. The shell is rotating at an angular velocity Ω about an axis $\mathbf{e}_z$, and its aspect ratio $r_i/r_o = 0.35$ is that of the present-day Earth's core. As the fluid is assumed to be incompressible, the continuity equation describes the velocity field $\mathbf{u}$ as solenoidal,

$$\nabla \cdot \mathbf{u} = 0. \tag{1}$$

Thermochemical convection is modeled by the codensity C (Braginsky and Roberts, 1995) in the Boussinesq approximation, such that

$$C = \alpha_T \rho T' + \Delta\rho \xi', \tag{2}$$

with α_T the thermal expansion coefficient, T' the deviation of the temperature field about the isentropic temperature, $\Delta\rho$ the density difference between light elements and pure iron and ξ' the light element mass fraction with respect to a well-mixed outer core. We assume that thermal and chemical diffusivities are both equal to κ, the codensity diffusivity, due to turbulent mixing in the outer core. Thus, the codensity field C is given by a single transport equation,

$$\frac{\partial C}{\partial t} + \mathbf{u} \cdot \nabla C = \kappa \nabla^2 C + S_{T/\xi}, \tag{3}$$

where $S_{T/\xi}$ is a volumetric correction term ensuring mass conservation (Aubert et al., 2009). To obtain the velocity $\mathbf{u}$, codensity C

and magnetic fields $\mathbf{B}$ we solve equations (1) and (3) together with the electromagnetic induction equation in the magnetohydrodynamic approximation and the Navier–Stokes equation accounting for the back reaction of the solenoidal magnetic field on the flow:

$$\frac{\partial \mathbf{B}}{\partial t} = \nabla \times (\mathbf{u} \times \mathbf{B}) + \eta \nabla^2 \mathbf{B}, \tag{4}$$

$$\rho \left(\frac{\partial \mathbf{u}}{\partial t} + \mathbf{u} \cdot \nabla \mathbf{u} \right) = -\nabla P - 2\rho (\boldsymbol{\Omega} \times \mathbf{u}) + \rho \nu \nabla^2 \mathbf{u} + \frac{1}{\mu_0} (\nabla \times \mathbf{B}) \times \mathbf{B} + \mathbf{g} C, \tag{5}$$

$$\nabla \cdot \mathbf{B} = 0. \tag{6}$$

This set of equations is solved in the planetary reference frame and gravitational acceleration $\mathbf{g}$ is directed along $\mathbf{e}_r$. The magnetic diffusivity of the fluid is defined as η and its magnetic permeability as μ_0.

We adopt stress-free conditions at both ICB and CMB, to mitigate the influence of viscosity on the fluid outer core boundaries. The viscosity is the least realistic parameter in numerical dynamo models, being overestimated by several orders of magnitude. This condition can be written

$$u_r \Big|_{r=r_i, r_o} = 0, \quad \text{and} \tag{7}$$

$$\frac{\partial}{\partial r} \left(\frac{u_\theta}{r} \right) \Big|_{r=r_i, r_o} = \frac{\partial}{\partial r} \left(\frac{u_\varphi}{r} \right) \Big|_{r=r_i, r_o} = 0. \tag{8}$$

The mass anomaly flux F is spatially homogeneous and remains constant over time at the inner core surface S_{ICB} and is taken as zero at the CMB so that

$$F = \int_{S_{ICB}} \kappa \nabla C \cdot \mathbf{dS}, \quad \text{and} \tag{9}$$

$$0 = \int_{S_{CMB}} \kappa \nabla C \cdot \mathbf{dS}, \tag{10}$$

with S_{CMB} the core–mantle boundary surface. This simulates a situation where convection is entirely bottom-driven, as would be the case if the CMB total heat flux were exactly adiabatic. The inner core is modeled as a rigid body, free to rotate at an angular velocity Ω_{ic} under the influence of electromagnetic and gravitational torques. We assume that the electrical conductivities of the fluid and the solid parts of the core are equal, and we denote them by σ_c. This greatly simplifies our model and appears a reasonable assumption in light of mineral physics estimates (Pozzo et al., 2012; de Koker et al., 2012; Gomi et al., 2013). The mantle is considered as conductive in a layer of thickness Δ and conductivity σ_m directly above the CMB. At radii greater than $r_o + \Delta$, the mantle is considered as insulating and the magnetic field is a potential field.

The angular momentum evolution in both inner core and mantle is determined by the torque balance between electromagnetic and gravitational coupling

$$I_m \frac{d\Omega_m}{dt} = -\Gamma_G + \Gamma_{CMB}, \tag{11}$$

$$I_i \frac{d\Omega_{ic}}{dt} = \Gamma_G + \Gamma_{ICB}, \tag{12}$$

with I_m and I_i respectively the moments of inertia of the mantle and the inner core. For the fluid outer core, the evolution of angular momentum can be written

$$\frac{d}{dt} \int_V \rho (r \sin\theta)^2 \omega_f dV = -\Gamma_{CMB} - \Gamma_{ICB}, \tag{13}$$

where V is the volume of the outer core and ω_f the local rotation rate of fluid parcels.

The electromagnetic torques acting on the mantle and the inner core, respectively Γ_{CMB} and Γ_{ICB}, can be evaluated following the formalism developed by Rochester (1960, 1962). The moment of the Lorentz force integrated over a given volume is thereby reduced to the integral of the product of the radial and azimuthal magnetic field, B_r and B_φ, over the surface of the core–mantle boundary for Γ_{CMB} and the surface of the inner core for Γ_{ICB}. The electromagnetic torques can then be written

$$\Gamma_{CMB} = -\frac{r_o}{\mu_0} \int_{S_{CMB}} B_r B_\varphi \sin\theta dS, \quad \text{and} \tag{14}$$

$$\Gamma_{ICB} = \frac{r_i}{\mu_0} \int_{S_{ICB}} B_r B_\varphi \sin\theta dS, \tag{15}$$

respectively. The restoring gravitational torque Γ_G exerted on the inner core is proportional to its misalignment angle ϕ relative to the mantle, and a gravitational coupling constant Γ (Buffett, 1997; Buffett and Glatzmaier, 2000) as

$$\Gamma_G = -\phi \Gamma. \tag{16}$$

At any given time, the evolution of this misalignment angle is governed by

$$\frac{d\phi}{dt} = \Omega_{ic} - \Omega_m - \frac{\phi}{\tau}, \tag{17}$$

with Ω_{ic} and Ω_m, respectively the solid-body rotation rates of the inner core and the mantle, and τ the viscous relaxation time of the inner core. Our focus on the long-term behavior of the geodynamo in this study allows us to adopt a simpler expression for ϕ. When the fluctuations of ϕ occur on time scales longer than the inner core relaxation time this gives $d\phi/dt \ll \phi/\tau$, and thus $\phi = (\Omega_{ic} - \Omega_m)\tau$ (Aubert and Dumberry, 2011). Introducing this expression into (16) leads to

$$\Gamma_G = -(\Omega_{ic} - \Omega_m)\tau \Gamma. \tag{18}$$

2.2. Dimensionless equations and numerical implementation

Since our study relies on the rotational dynamics of the geodynamo we choose Ω^{-1}, the inverse of the planetary rotation rate, as the relevant timescale. The length scale is D, the thickness of the fluid shell. Magnetic induction B is scaled by $(\rho\mu_0)^{1/2}\Omega D$ and the non-hydrostatic pressure by $\rho\Omega^2 D^2$, following the study of Christensen and Aubert (2006). Finally, the codensity C is scaled with $F/4\pi D^3 \Omega$ (Aubert et al., 2009). For simplicity, we adopt in the following sections the same notation for dimensionless variables as for our previously defined dimensional variables. From herein, equations and results will be presented in dimensionless form. Governing equations can then be written as

$$\frac{\partial \mathbf{u}}{\partial t} + \mathbf{u} \cdot \nabla \mathbf{u} + \nabla P + 2\mathbf{e_z} \times \mathbf{u} = E \nabla^2 \mathbf{u} + (\nabla \times \mathbf{B}) \times \mathbf{B} + \frac{\mathbf{r}}{r_o} \mathcal{R} a_F C, \tag{19}$$

$$\frac{\partial C}{\partial t} + \mathbf{u} \cdot \nabla C = E_\kappa \nabla^2 C + S_{T/\xi}, \tag{20}$$

$$\frac{\partial \mathbf{B}}{\partial t} - \nabla \times (\mathbf{u} \times \mathbf{B}) = E_\eta \nabla^2 \mathbf{B}. \tag{21}$$

The four non-dimensional parameters are the Ekman number,

$$E = \frac{\nu}{\Omega D^2}, \tag{22}$$

the thermochemical Ekman number,

$$E_\kappa = \frac{\kappa}{\Omega D^2}, \tag{23}$$

the magnetic Ekman number,

$$E_\eta = \frac{\eta}{\Omega D^2}, \tag{24}$$

and the modified Rayleigh number,

$$\mathcal{R}a_F = \frac{g_o F}{4\pi\rho\Omega^3 D^4}, \tag{25}$$

accounting for a fixed-flux boundary condition at the inner core surface, with g_o the gravitational acceleration at the CMB. Values of the input parameters for the 45 models considered in this study are summarized in Tables 1 and 2.

In dimensionless form, equations (11) and (12) now become

$$\mathrm{I_m}\frac{\mathrm{d}\Omega_\mathrm{m}}{\mathrm{dt}} = \zeta\,(\Omega_\mathrm{ic} - \Omega_\mathrm{m}) + \frac{\Gamma_\mathrm{CMB}}{\rho D^5\Omega^2}, \tag{26}$$

$$\mathrm{I_i}\frac{\mathrm{d}\Omega_\mathrm{ic}}{\mathrm{dt}} = -\zeta\,(\Omega_\mathrm{ic} - \Omega_\mathrm{m}) + \frac{\Gamma_\mathrm{ICB}}{\rho D^5\Omega^2}, \tag{27}$$

with Γ_CMB and Γ_ICB as defined by equations (14) and (15). This system includes a new dimensionless parameter, ζ, representing the strength of the gravitational coupling between the inner core and the mantle. As moments of inertia are scaled using ρD^5 and electromagnetic torques using $\rho D^5\Omega^2$, this gives

$$\zeta = \frac{\tau\Gamma}{\rho D^5\Omega}. \tag{28}$$

Given our choice of characteristic scales, ζ is normalized by the fluid core angular momentum, it thus compares the relative importance of gravitational coupling and core inertia.

Finally, it is important to mention one last dimensionless parameter that does not directly appear in the equations but which enters the formulation of the CMB magnetic boundary condition, namely the parameter

$$\Sigma = \frac{\Delta\sigma_\mathrm{m}}{D\sigma_\mathrm{c}}. \tag{29}$$

The parameter Σ compares the relative importance of mantle and core conductances. It should be kept in mind that while values of ζ of $\mathcal{O}(1)$ are geophysically admissible, values of Σ of the same order are clearly unrealistic such that in general $\Sigma \ll 1$. The mantle is indeed a poor electrical conductor (see e.g. Civet et al., 2015 and references therein), at the exception (already discussed in the introduction) of a thin layer above the CMB (Ohta et al., 2008; Ohta et al., 2012) whose conductance may reach the value of 10^8 S inferred by Buffett (1992). This last value is four orders of magnitude lower than the fluid core conductance. We can therefore anticipate that the geophysically relevant range for Σ does not extend beyond 10^{-3}. For the sake of completeness, however, the range we shall consider in this study covers 7 orders of magnitude, with Σ varying from 10^{-8} to 10^{-1}.

We performed numerical 45 simulations of the system (19)–(29) using the PARODY-JA numerical implementation (Dormy et al., 1998; Aubert et al., 2008), the latest version of which uses the spectral transform library SHTns (Schaeffer, 2013). Tables 1 and 2 summarize the input and output parameters of the parameter space survey. Among the outputs not yet defined, we mention here: $AD/(AD+NAD)$, the relative axial dipole power defined by Christensen et al. (2010), L_max, the maximum degree and order of the spherical harmonic decomposition in the horizontal directions, the number of grid points in the radial direction NR, and the mean squared magnetic field respectively at ICB and CMB, $B^2_{r_i}$ and $B^2_{r_o}$. Most dynamos exhibit a strong dipolar component, i.e. $AD/(AD+NAD) \geq 0.6$. Since we are mainly interested in the long-term (time-average) behavior of the system, simulations were time-integrated as to ensure convergence of time-averages for the values of interest (see Tables 1 and 2).

2.3. Theoretical analysis of the long-term rotational state

Before inspecting the results of our set of 45 simulations, we dedicate this section to the theoretical description of the long-term rotational dynamics of our system, the predictions of which will be tested against numerical results in section 3. As shown in Fig. 1, this long-term dynamics can be described using 4 rotation rates: Ω_ic, Ω_m, Ω_ficb and Ω_fcmb, respectively the solid-body angular rotation rates of the inner core, the mantle, the fluid at the ICB and the fluid at the CMB. Recall indeed that stress-free boundary conditions allow for velocity jumps at the fluid outer core boundaries. At the ICB, this velocity jump is denoted as

$$\mathcal{C}_\mathrm{icb} = \langle\Omega_\mathrm{ficb} - \Omega_\mathrm{ic}\rangle, \tag{30}$$

the angle brackets $\langle\ \rangle$ meaning time-average quantities. Similarly,

$$\mathcal{D} = \langle\Omega_\mathrm{fcmb} - \Omega_\mathrm{m}\rangle, \tag{31}$$

denotes the equivalent at the CMB, the long-term geomagnetic westward drift. In addition, we define

$$\mathcal{S} = \langle\Omega_\mathrm{ic} - \Omega_\mathrm{m}\rangle, \tag{32}$$

the long-term inner core super-rotation, and

$$\mathcal{C}_\mathrm{f} = \langle\Omega_\mathrm{ficb} - \Omega_\mathrm{fcmb}\rangle, \tag{33}$$

the long-term global convective shear linking the two boundaries. The formal link between the four quantities is then

$$\mathcal{C}_\mathrm{f} = \mathcal{C}_\mathrm{icb} + \mathcal{S} - \mathcal{D}. \tag{34}$$

To derive the link between the long-term geomagnetic westward drift $\mathcal{D}$ and the long-term differential rotation of the inner core $\mathcal{S}$, the intuitive first step is then to relate the four components of the rotational dynamics expressed above to the strengths of the electromagnetic and gravitational torques (Eqs. (14), (15), (18)), and use the fact that these torques should balance when considering the long-term conservation of angular momentum. Therefore, we approximate the time-average electromagnetic torques, $\langle\Gamma_\mathrm{CMB}\rangle$ and $\langle\Gamma_\mathrm{ICB}\rangle$, using the theoretical approach developed by Dumberry (2007). At the CMB, this theory relies on a thin layer approximation (Stewart et al., 1995; Holme, 1998) and the torque thus results from a simple shear of the poloidal field by the westward drift. The torque is then directly proportional to the lower mantle conductance $\Delta\sigma_\mathrm{m}$, to the mean squared magnetic field at CMB $\left(B^2_{r_o}\right)$ and to $\mathcal{D}$. In dimensional form this leads to

$$\langle\Gamma_\mathrm{CMB}\rangle \simeq K_1 r_o^4 B^2_{r_o}\Delta\sigma_\mathrm{m}\mathcal{D}, \tag{35}$$

with K_1 a numerical constant to be determined (see section 3.3). In dimensionless form this gives

$$\langle\Gamma_\mathrm{CMB}\rangle \simeq \frac{K_1}{E_\eta} r_o^4 B^2_{r_o}\Sigma\mathcal{D}. \tag{36}$$

In contrast to the situation at the CMB, modeling the electromagnetic torque at the ICB is more complex, in particular because the inner core is not a thin flat layer. Aurnou et al. (1996, 1998) highlighted that the consequence of this thick-layer configuration is that the azimuthal magnetic field initiating the torque is now made of two contributions: one due to the local shear at the ICB, and the other due to the shear in the tangent cylinder, resulting from the thermal wind balance. This idea was further explored by Dumberry (2007) through an analytical solution, allowing an estimate of the ratio between these two contributions from the shear

Table 1
Parameters of the numerical simulations. All runs were performed with $E = E_\kappa = 3 \times 10^{-5}$ and $E_\eta = 1.2 \times 10^{-5}$. Labels A, B, C and D correspond to numerical simulations displayed in Figs. 2 and 3.

	$\mathcal{R}a_F$	Σ	ζ	$\mathcal{D}$	$\mathcal{C}_\mathrm{f}$	$\mathcal{C}_\mathrm{icb}$	$\mathcal{S}$	$B^2_{r_i}$	$B^2_{r_o}$	$\frac{AD}{AD+NAD}$	NR	L_max
	2.70×10^{-5}	1.00×10^{-8}	0.75	-5.30×10^{-3}	0.01	5.02×10^{-3}	2.76×10^{-6}	4.40×10^{-4}	1.01×10^{-5}	0.66	120	85
	2.70×10^{-5}	1.00×10^{-7}	0.75	-5.04×10^{-3}	0.01	5.20×10^{-3}	2.78×10^{-6}	4.59×10^{-4}	9.42×10^{-6}	0.65	120	85
	2.70×10^{-5}	1.00×10^{-6}	0.75	-5.49×10^{-3}	0.01	4.75×10^{-3}	2.77×10^{-6}	4.65×10^{-4}	1.04×10^{-5}	0.67	120	85
	2.70×10^{-5}	1.00×10^{-5}	0.75	-5.27×10^{-3}	0.01	5.27×10^{-3}	3.54×10^{-6}	4.72×10^{-4}	1.01×10^{-5}	0.66	120	85
	2.70×10^{-5}	5.00×10^{-5}	0.75	-4.36×10^{-3}	0.01	5.76×10^{-3}	5.75×10^{-6}	4.62×10^{-4}	9.75×10^{-6}	0.65	120	85
	2.70×10^{-5}	1.00×10^{-4}	0.75	-3.99×10^{-3}	9.93×10^{-3}	5.93×10^{-3}	8.82×10^{-6}	4.51×10^{-4}	1.07×10^{-5}	0.67	120	85
	2.70×10^{-5}	1.00×10^{-3}	0.75	-1.50×10^{-3}	9.41×10^{-3}	7.89×10^{-3}	1.97×10^{-5}	4.75×10^{-4}	1.39×10^{-5}	0.63	120	85
	2.70×10^{-5}	5.00×10^{-3}	0.75	-8.17×10^{-4}	0.01	9.22×10^{-3}	2.49×10^{-5}	4.54×10^{-4}	6.19×10^{-5}	0.58	120	85
	2.70×10^{-5}	0.01	0.75	-7.58×10^{-4}	0.01	0.01	2.29×10^{-5}	3.95×10^{-4}	1.21×10^{-4}	0.50	120	85
	2.70×10^{-5}	0.05	0.75	-4.36×10^{-4}	0.01	0.01	2.09×10^{-5}	3.22×10^{-4}	4.38×10^{-4}	0.21	120	85
(D)	2.70×10^{-5}	0.10	0.75	-2.10×10^{-4}	0.01	0.01	1.75×10^{-5}	3.08×10^{-4}	5.64×10^{-4}	0.05	120	85
	2.70×10^{-5}	1.00×10^{-4}	0	1.23×10^{-3}	0.01	4.22×10^{-3}	7.40×10^{-3}	4.66×10^{-4}	1.03×10^{-5}	0.67	120	85
	2.70×10^{-5}	1.00×10^{-4}	3.00×10^{-4}	-7.27×10^{-5}	0.01	4.84×10^{-3}	5.49×10^{-3}	4.55×10^{-4}	9.89×10^{-6}	0.66	120	85
	2.70×10^{-5}	1.00×10^{-4}	1.50×10^{-3}	-2.02×10^{-3}	0.01	5.57×10^{-3}	2.75×10^{-3}	4.84×10^{-4}	1.05×10^{-5}	0.66	120	85
	2.70×10^{-5}	1.00×10^{-4}	3.00×10^{-3}	-2.78×10^{-3}	0.01	5.66×10^{-3}	1.67×10^{-3}	4.85×10^{-4}	1.04×10^{-5}	0.66	120	85
	2.70×10^{-5}	1.00×10^{-4}	7.50×10^{-3}	-3.31×10^{-3}	0.01	5.96×10^{-3}	7.45×10^{-4}	4.60×10^{-4}	1.02×10^{-5}	0.66	120	85
	2.70×10^{-5}	1.00×10^{-4}	0.02	-3.63×10^{-3}	0.01	6.33×10^{-3}	3.88×10^{-4}	4.51×10^{-4}	9.75×10^{-6}	0.64	120	85
	2.70×10^{-5}	1.00×10^{-4}	0.03	-3.62×10^{-3}	0.01	6.19×10^{-3}	1.93×10^{-4}	4.53×10^{-4}	9.70×10^{-6}	0.65	120	85
	2.70×10^{-5}	1.00×10^{-4}	0.05	-3.80×10^{-3}	0.01	6.08×10^{-3}	1.20×10^{-4}	5.01×10^{-4}	1.05×10^{-5}	0.66	120	85
	2.70×10^{-5}	1.00×10^{-4}	0.07	-3.77×10^{-3}	9.87×10^{-3}	6.01×10^{-3}	8.23×10^{-5}	4.57×10^{-4}	1.02×10^{-5}	0.65	120	85
	2.70×10^{-5}	1.00×10^{-4}	0.15	-3.90×10^{-3}	0.01	6.21×10^{-3}	4.16×10^{-5}	4.70×10^{-4}	9.92×10^{-6}	0.66	120	85
	2.70×10^{-5}	1.00×10^{-4}	0.30	-3.89×10^{-3}	0.01	6.29×10^{-3}	2.06×10^{-5}	4.20×10^{-4}	9.92×10^{-6}	0.65	120	85
	2.70×10^{-5}	1.00×10^{-4}	0.45	-3.75×10^{-3}	9.99×10^{-3}	6.24×10^{-3}	1.30×10^{-5}	4.78×10^{-4}	9.66×10^{-6}	0.64	120	85
	2.70×10^{-5}	1.00×10^{-4}	0.60	-3.91×10^{-3}	0.01	6.34×10^{-3}	1.03×10^{-5}	4.35×10^{-4}	9.90×10^{-6}	0.65	120	85
	9.00×10^{-6}	1.00×10^{-4}	3.00×10^{-3}	-2.34×10^{-3}	5.97×10^{-3}	2.54×10^{-3}	1.09×10^{-3}	3.75×10^{-4}	9.90×10^{-6}	0.79	120	85
	1.35×10^{-5}	1.00×10^{-4}	3.00×10^{-3}	-2.63×10^{-3}	7.72×10^{-3}	3.79×10^{-3}	1.29×10^{-3}	4.13×10^{-4}	1.03×10^{-5}	0.74	120	85
	1.80×10^{-5}	1.00×10^{-4}	3.00×10^{-3}	-2.80×10^{-3}	8.88×10^{-3}	4.67×10^{-3}	1.41×10^{-3}	4.32×10^{-4}	1.01×10^{-5}	0.71	120	85
	2.25×10^{-5}	1.00×10^{-4}	3.00×10^{-3}	-2.75×10^{-3}	9.58×10^{-3}	5.31×10^{-3}	1.52×10^{-3}	4.55×10^{-4}	1.03×10^{-5}	0.68	120	85
(A)	2.70×10^{-5}	1.00×10^{-4}	0	-5.68×10^{-5}	0.01	4.14×10^{-3}	6.41×10^{-3}	4.82×10^{-4}	1.05×10^{-5}	0.68	220	85
	2.25×10^{-5}	1.00×10^{-4}	0	-1.55×10^{-4}	9.95×10^{-3}	3.91×10^{-3}	5.88×10^{-3}	4.79×10^{-4}	1.08×10^{-5}	0.71	220	85
	1.80×10^{-5}	1.00×10^{-4}	0	-1.78×10^{-4}	8.91×10^{-3}	3.29×10^{-3}	5.45×10^{-3}	4.65×10^{-4}	1.11×10^{-5}	0.73	220	85
	1.35×10^{-5}	1.00×10^{-4}	0	-2.10×10^{-4}	7.67×10^{-3}	2.77×10^{-3}	4.69×10^{-3}	4.36×10^{-4}	1.09×10^{-5}	0.76	220	85
	9.00×10^{-6}	1.00×10^{-4}	0	-2.67×10^{-4}	6.03×10^{-3}	1.93×10^{-3}	3.84×10^{-3}	3.84×10^{-4}	1.02×10^{-5}	0.79	220	85
	6.30×10^{-5}	1.00×10^{-4}	0	1.50×10^{-3}	8.39×10^{-3}	3.11×10^{-3}	6.78×10^{-3}	6.21×10^{-4}	1.29×10^{-5}	0.62	220	85
	7.20×10^{-5}	1.00×10^{-4}	0	1.96×10^{-3}	5.95×10^{-3}	1.95×10^{-3}	5.95×10^{-3}	6.97×10^{-4}	1.49×10^{-5}	0.65	220	85
	2.70×10^{-5}	1.00×10^{-4}	0.75	-4.14×10^{-3}	0.01	6.22×10^{-3}	7.45×10^{-6}	4.57×10^{-4}	9.69×10^{-6}	0.65	140	85
	2.70×10^{-5}	1.00×10^{-4}	0.75	-4.25×10^{-3}	9.95×10^{-3}	5.69×10^{-3}	7.97×10^{-6}	4.88×10^{-4}	1.09×10^{-5}	0.67	160	85
	2.70×10^{-5}	1.00×10^{-4}	0.75	-4.33×10^{-3}	0.01	5.78×10^{-3}	7.22×10^{-6}	4.76×10^{-4}	1.03×10^{-5}	0.67	180	85
	2.70×10^{-5}	1.00×10^{-4}	0.75	-4.36×10^{-3}	0.01	5.69×10^{-3}	7.31×10^{-6}	4.79×10^{-4}	1.05×10^{-5}	0.67	200	85
(C)	2.70×10^{-5}	1.00×10^{-4}	0.75	-4.40×10^{-3}	0.01	5.94×10^{-3}	6.91×10^{-6}	4.76×10^{-4}	1.03×10^{-5}	0.66	220	85
	2.70×10^{-5}	1.00×10^{-4}	0.75	-4.40×10^{-3}	0.01	5.88×10^{-3}	6.48×10^{-6}	4.68×10^{-4}	9.84×10^{-6}	0.66	240	85
(B)	2.70×10^{-5}	1.00×10^{-8}	0.75	-5.92×10^{-3}	0.01	4.72×10^{-3}	4.93×10^{-7}	4.59×10^{-4}	9.70×10^{-6}	0.67	220	85

Table 2
Parameters of the numerical simulations with $E = E_\kappa = 1 \times 10^{-5}$.

E_η	$\mathcal{R}a_F$	Σ	ζ	$\mathcal{D}$	$\mathcal{C}_f$	$\mathcal{C}_{icb}$	$\mathcal{S}$	$B^2_{r_i}$	$B^2_{r_o}$	$\frac{AD}{AD+NAD}$	NR	L_{max}
4.00×10^{-6}	3.00×10^{-6}	1.00×10^{-4}	0	2.06×10^{-5}	3.50×10^{-3}	1.72×10^{-3}	1.80×10^{-3}	2.34×10^{-4}	7.07×10^{-6}	0.70	240	133
6.67×10^{-6}	9.00×10^{-6}	1.00×10^{-4}	0	-2.59×10^{-4}	7.47×10^{-3}	3.42×10^{-3}	3.80×10^{-3}	2.24×10^{-4}	4.71×10^{-6}	0.64	240	170
6.67×10^{-6}	2.00×10^{-5}	1.00×10^{-4}	0	7.47×10^{-4}	7.69×10^{-3}	3.89×10^{-3}	4.55×10^{-3}	2.19×10^{-4}	2.69×10^{-6}	0.45	240	170

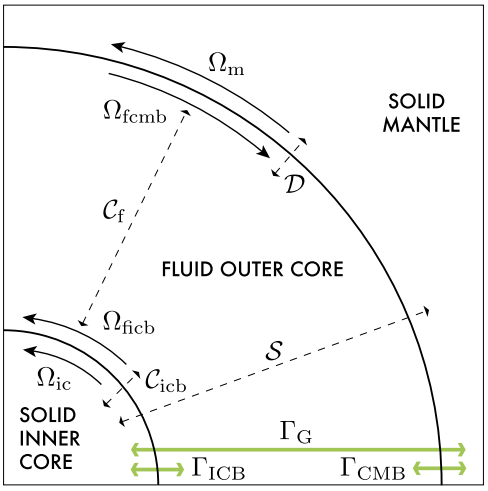

Fig. 1. Rotational state of our system. Black arrowed lines define rotation rates: Ω_m is the angular velocity of the solid mantle, Ω_{fcmb} (resp. Ω_{ficb}) is the rotation rate of the fluid outer core in the vicinity of the CMB (resp. the ICB), and Ω_{ic} is the angular velocity of the solid inner core. Dashed lines represent the various time-average shears: $\mathcal{D}$ is the long-term westward drift (Eq. (31)), $\mathcal{S}$ is the long-term inner core differential rotation (Eq. (32)), $\mathcal{C}_f$ is the long-term shear available in the fluid outer core (Eq. (33)), and $\mathcal{C}_{icb}$ denotes the long-term shear at the ICB (Eq. (30)). Green lines indicate torques. Γ_{CMB} (resp. Γ_{ICB}) is the electromagnetic torque at the CMB (resp. the ICB), and Γ_G is the gravitational torque exerted by the mantle on the inner core. (For interpretation of the references to color in this figure legend, the reader is referred to the web version of this article.)

at the ICB, $\mathcal{C}_{icb}$, and in the fluid, $\mathcal{C}_f$. This enables the formulation of the following dimensional model of the electromagnetic torque acting on the inner core,

$$\langle \Gamma_{ICB} \rangle \simeq K_2 \sigma_c r_i^5 B^2_{r_i} (\mathcal{C}_{icb} - \alpha \mathcal{C}_f) \tag{37}$$

with α representing the relative amplitude between the two contributions and K_2 another numerical constant to be determined (see section 3.3). The dimensionless form of this model is then

$$\langle \Gamma_{ICB} \rangle \simeq \frac{K_2}{E_\eta} r_i^5 B^2_{r_i} (\mathcal{C}_{icb} - \alpha \mathcal{C}_f) . \tag{38}$$

Equation (38) reflects that in a situation where there is no restoring torque to balance $\langle \Gamma_{ICB} \rangle$, so that $\langle \Gamma_{ICB} \rangle = 0$, the local and remote contributions to the electromagnetic torque cancel and

$$\alpha = \frac{\mathcal{C}_{icb}}{\mathcal{C}_f} . \tag{39}$$

Finally, the time-average dimensionless gravitational torque exerted on the inner core is directly proportional to the long-term inner core super-rotation (Eq. (32)),

$$\langle \Gamma_G \rangle = -\mathcal{S}\zeta . \tag{40}$$

Assuming that the laws described by equations (36) and (38) hold in numerical models of the geodynamo (see section 3.3 below for a detailed analysis), the long-term conservation of the angular momentum of the mantle and inner core (Eqs. (26), (27)) now become

$$0 = \zeta \mathcal{S} + \frac{K_1}{E_\eta} r_o^4 B^2_{r_o} \Sigma \mathcal{D}, \quad \text{and} \tag{41}$$

$$0 = -\zeta \mathcal{S} + \frac{K_2}{E_\eta} r_i^5 B^2_{r_i} (\mathcal{C}_{icb} - \alpha \mathcal{C}_f) , \quad \text{respectively.} \tag{42}$$

Equation (41) can lead to a first statement of the inner core super-rotation. We have

$$\mathcal{S} = -\frac{1}{\epsilon_1} \mathcal{D}, \quad \text{with} \tag{43}$$

$$\epsilon_1 = \frac{\zeta E_\eta}{K_1 r_o^4 B^2_{r_o} \Sigma} . \tag{44}$$

Another expression of $\mathcal{S}$ can be obtained using the ICB torque balance (42):

$$\mathcal{S} = \frac{1}{\epsilon_2} (\mathcal{C}_{icb} - \alpha \mathcal{C}_f) , \quad \text{with} \tag{45}$$

$$\epsilon_2 = \frac{\zeta E_\eta}{K_2 r_i^5 B^2_{r_i}} . \tag{46}$$

The meaning of the two parameters ϵ_1 and ϵ_2 is the following: ϵ_1 is the ratio between the gravitational and the electromagnetic coupling strength exerted on the mantle, and ϵ_2 describes the same ratio applied to the inner core. We re-express equations (43) and (45) using the global convective shear $\mathcal{C}_f$ as a control parameter. Then, from the decomposition of equation (34) we can express the westward drift and the inner core super-rotation as

$$\mathcal{D} = -\frac{\epsilon_1 (1-\alpha) \mathcal{C}_f}{1 + \epsilon_1 + \epsilon_2}, \quad \text{and} \tag{47}$$

$$\mathcal{S} = \frac{(1-\alpha) \mathcal{C}_f}{1 + \epsilon_1 + \epsilon_2} . \tag{48}$$

Finally, we can formulate the link between $\mathcal{S}$ and $\mathcal{D}$ through an equation describing the repartition of the total shear of the system:

$$\mathcal{S} - \mathcal{D} = (1-\alpha) \mathcal{C}_f \frac{1 + \epsilon_1}{1 + \epsilon_1 + \epsilon_2} . \tag{49}$$

Recall that the validity of this model will be checked against numerical simulations in section 3, where we will determine the values of the numerical constants K_1, K_2, and α.

2.4. Thermal wind scaling of the convective shear $\mathcal{C}_f$

Equations (47)–(49) suggest that the strengths of both $\mathcal{S}$ and $\mathcal{D}$ are controlled by the state of coupling (i.e. ϵ_1 and ϵ_2), and by $\mathcal{C}_f$, the mean shear in the fluid outer core. This shear is a control parameter because it should only depend on the vigor of the convection, embodied by the Rayleigh number $\mathcal{R}a_F$ (Eq. (25)). This assumption stems from the thermal wind balance between Coriolis, buoyancy and pressure forces. Considered inside the tangent cylinder, this balance is thought to control the average inner core super-rotation (Aurnou et al., 1996, 1998) and more generally the convective shear $\mathcal{C}_f$. Taking $[\nabla \times (5)] \cdot \mathbf{e}_\varphi$, the thermal wind steady-state azimuthal velocity obeys

$$\frac{\partial u_\varphi}{\partial z} = \frac{g}{2 r \rho \Omega} \frac{\partial C}{\partial \theta}, \tag{50}$$

in dimensional form. Introducing a typical velocity $U \simeq \mathcal{C}_f D$, a typical advective co-density perturbation can then be evaluated as $C \simeq F / 4\pi D^2 U$. Dimensional analysis of equation (50) then yields

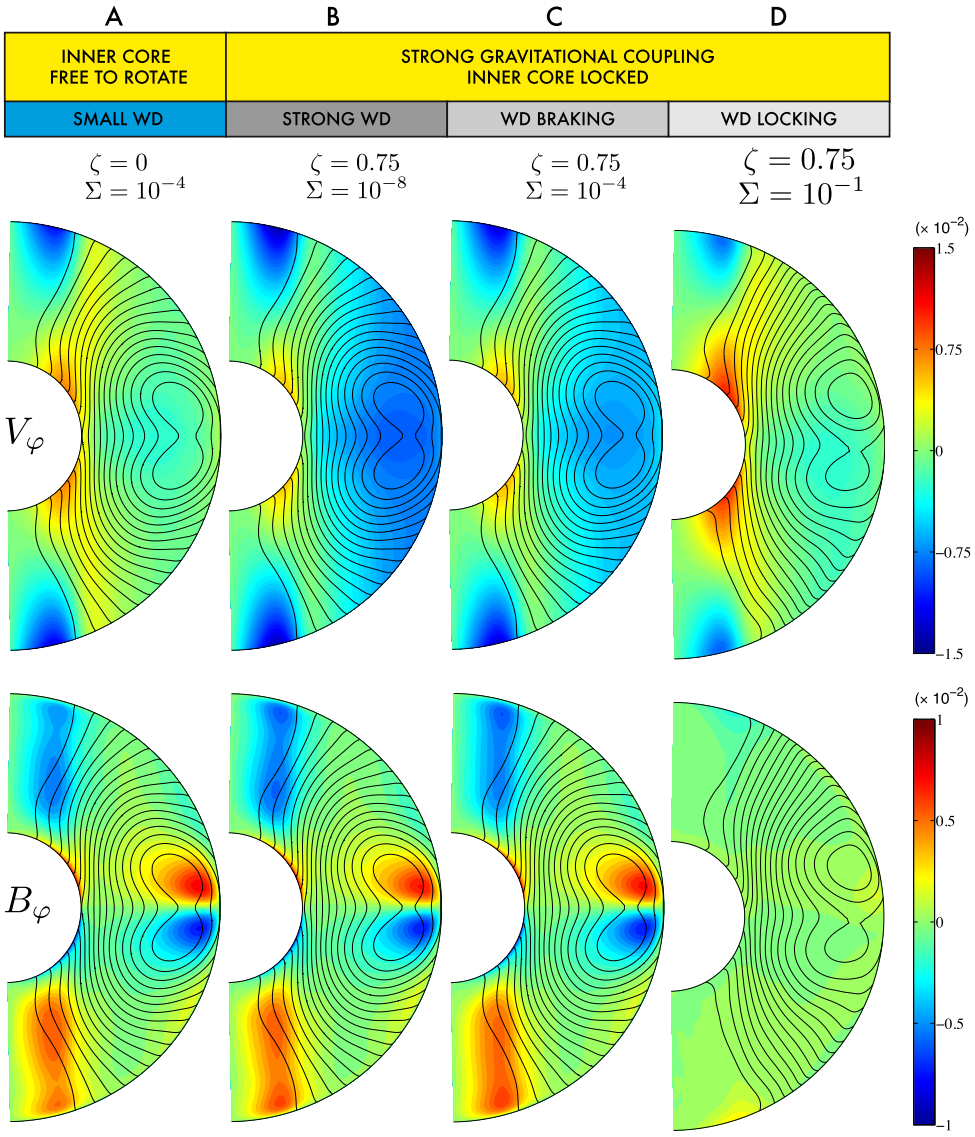

Fig. 2. Meridional sections of the time and longitude-averaged azimuthal velocity V_φ (top-panel) and the azimuthal magnetic field B_φ (bottom-panel) of the numerical simulations highlighted in Table 1 (rows A, B, C and D). Black lines represent the axisymmetric poloidal magnetic field lines. The WD acronym stands for Westward Drift.

$$\mathcal{C}_\mathrm{f}^2 \simeq \frac{1}{2\theta}\frac{gF}{4\pi\rho\Omega D^4}. \tag{51}$$

Using the tangent cylinder angle $\theta = 0.36$ rad, this gives in dimensionless form

$$\mathcal{C}_\mathrm{f} \simeq 1.2\,\mathcal{R}a_F^{\frac{1}{2}}, \tag{52}$$

the classical thermal wind scaling (Aurnou et al., 2003; Aubert, 2005), the validity of which will be examined in section 3.2.

3. Results

We analyze now the long-term rotational state of our set of 45 simulations (see Tables 1 and 2), and in particular the influence of the two control parameters Σ and ζ. In order to obtain a satisfying parameters survey and end-member cases, we first present the results of numerical simulations with Σ varying from 10^{-8} to 10^{-1}, corresponding to a lower mantle conductance up to one order of magnitude below the fluid core conductance, and simulations with ζ varying from 0 to 0.75, this last value being sufficient to lock the whole system by gravitational coupling (Aubert et al., 2013).

3.1. Typical long-term state of differential rotations

The purpose of this section is to examine the behavior of our system, in terms of the intensity and geometry of both the field and flow. We first focus on four typical cases presented in Fig. 2. Fig. 2 (top-panel) shows the long-term patterns of the average azimuthal velocities which shear the ambient meridional magnetic field lines to produce the azimuthal field presented in Fig. 2 (bottom-panel). At both the ICB and the CMB, this interaction is the source of electromagnetic torques. The long-term rotational state ($\mathcal{D}$, $\mathcal{S}$, $\mathcal{C}_\mathrm{icb}$, $\mathcal{C}_\mathrm{f}$) corresponding to cases A, B, C and D presented in Fig. 2 is further detailed in Fig. 3. In case A (Fig. 2), the gravitational coupling between the inner core and the mantle is set to zero. Thus, the inner core is free to rotate and the inner core super-rotation is at its peak (see Fig. 3b). Moreover, the westward drift of fluid close to the CMB is small. For the other cases B, C and D (Fig. 2), the gravitational coupling is comparable to core inertia and the inner core rotation is braked such that, on average, $\mathcal{S}$ is almost zero (see Fig. 3a). We can thus focus on the influence of the lower mantle conductivity. Case B has a strong westward drift since the lower mantle conductance is almost insignificant ($\Sigma \ll 1$). As Σ is increased, the westward drift is significantly low-

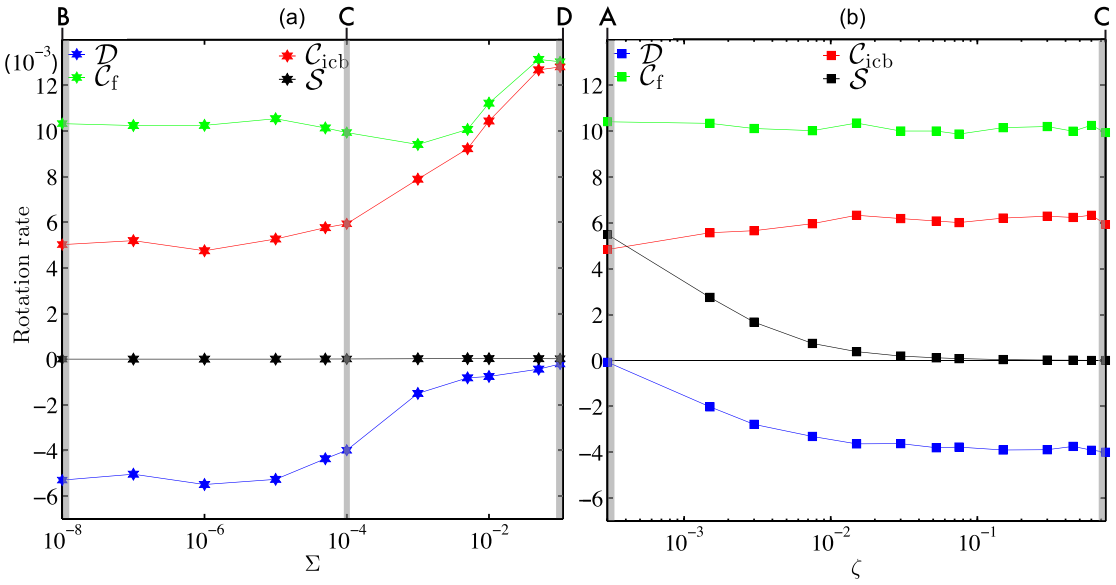

Fig. 3. Time-average differential rotations $\mathcal{C}_{\rm icb}$, $\mathcal{D}$, $\mathcal{S}$ and $\mathcal{C}_{\rm f}$ (see Eqs. (30), (31), (32), (33)) as functions of the mantle conductance Σ (with $\zeta = 0.75$) (a) and the gravitational coupling strength ζ (with $\Sigma = 10^{-4}$) (b), in a set of numerical simulations where $\mathcal{R}a_F = 3 \times 10^4$, $E = 3 \times 10^{-5}$ and $E_\eta = 1.2 \times 10^{-5}$. Labels A, B, C and D refer to simulations of Fig. 2 (see also Table 1).

ered (case C), down to a point where the fluid close to the CMB is completely locked to the mantle through electromagnetic coupling (case D). The increase of Σ also triggers an increase of the shear close to the ICB, mostly occurring in the tangent cylinder. Finally, comparing cases A and C, we can already envision a link between $\mathcal{S}$ and $\mathcal{D}$. As a matter of fact, for the same lower mantle conductance, a change in the mean differential rotation of the inner core caused by a variation of the gravitational torque also induces a pronounced change in the azimuthal velocity of the fluid close to the CMB. This is achieved while preserving the thermal wind shear between the CMB and the ICB within the tangent cylinder (see shear patterns in Fig. 2, top-panel, and the stability of $\mathcal{C}_{\rm f}$ in Fig. 3a, b).

The systematic impact of the mantle conductance Σ and the gravitational coupling strength ζ is further explored in Fig. 3. Fig. 3a presents the results of the time-average characteristic rotation rates of our system, in a situation where the inner core and the mantle are strongly gravitationally coupled. In that case, the inner core is indeed completely locked to the mantle, so that $\mathcal{S}$ is vanishingly small. At low values of mantle conductance, the fluid below the CMB reaches its peak westward rotation rate ($\mathcal{D}$ is maximum), whereas the fluid close to the ICB is rotating eastward ($\mathcal{C}_{\rm icb} > 0$). For increasing values of mantle conductance, the strength of the electromagnetic coupling between the mantle and the fluid core increases as well. This results in a decrease of $\mathcal{D}$, as the fluid close to the CMB tends to be more and more locked to the mantle, as observed already in Fig. 2. Remarkably, the shear $\mathcal{C}_{\rm f}$ in the whole fluid core is confirmed to be roughly constant, over a wide range of mantle conductance. A decreasing $\mathcal{D}$ is thus accompanied by an increasing eastward rotation of the fluid close to the ICB, and therefore a higher local shear $\mathcal{C}_{\rm icb}$, since the inner core differential rotation rate $\mathcal{S}$ remains close to zero. Fig. 3b displays the effects of the strength of gravitational coupling between the mantle and the inner core, on the rotational dynamics of the system. At low ζ, the inner core is free to rotate. It is therefore entrained in a substantial eastward rotation by the fluid close to the ICB, through electromagnetic coupling. As ζ is increased, the inner core rotation is progressively braked until a situation of gravitational locking with the mantle, so that $\mathcal{S}$ almost vanishes (Fig. 3b). Just as previously (Fig. 3a), the shear in the fluid $\mathcal{C}_{\rm f}$ remains constant. As a consequence, the increase of the shear at the ICB, triggered by the braking of the inner core super-rotation, is balanced by an increase of the westward motion of the fluid close to the CMB. The key observation in Figs. 2 and 3 is the stability of the global shear $\mathcal{C}_{\rm f}$ available in the fluid core. Consequently, any modification of a physical control parameter or directly of fluid flow close to the CMB directly impacts the fluid close to the ICB and the inner core axial rotation rate. This observation is thus crucial to formulate the link between $\mathcal{S}$ and $\mathcal{D}$ (Eqs. (47)–(49)), and their respective dependency on the global convective shear $\mathcal{C}_{\rm f}$.

3.2. Thermal wind scaling of $\mathcal{C}_{\rm f}$

We have seen that $\mathcal{C}_{\rm f}$ is largely independent on the state of coupling at the boundaries. The leading control of the convection vigor on $\mathcal{C}_{\rm f}$ (Eq. (52)) is now tested against our numerical dataset in Fig. 4. Equation (52) is found to be valid at low values of $\mathcal{R}a_F$ with a prefactor rather close to the theoretical value of 1.2,

$$\mathcal{C}_{\rm f} = 2.01\, \mathcal{R}a_F^{\frac{1}{2}}. \tag{53}$$

The thermal wind scaling is expected to no longer hold at high values of $\mathcal{R}a_F$ because inertia starts to disrupt the force balance. In our numerical simulations, this occurs rather quickly, due to the modest values of the Ekman number, leading to high Rossby numbers, at which our simulations are calculated. Lower Ekman numbers should presumably allow for more inertia before the thermal wind balance is disrupted, thus extending the range of validity of equation (52).

3.3. Long-term electromagnetic torques

We next turn to the analysis of the CMB electromagnetic torque $\langle \Gamma_{\rm CMB} \rangle$. In Fig. 5, we verify first that the linear relationship suggested by equation (36) is valid in the range $0 < \Sigma < 3.07 \times 10^{-4}$, with $K_1 = 2.3$, determined by least-squares regression. For values of Σ beyond $\Sigma_{\rm c}$, we observe a saturation of the electromagnetic torque. This is due to the fact that this torque, as defined by equation (36), is necessarily limited in a self-sustained, power-limited dynamo where the magnetic field strength itself is bounded. For $\Sigma > \Sigma_{\rm c}$ also, the saturation of the CMB electromagnetic torque then implies a decreasing amplitude for the westward drift $\mathcal{D}$. From here, we thus exclude these numerical simulations for which

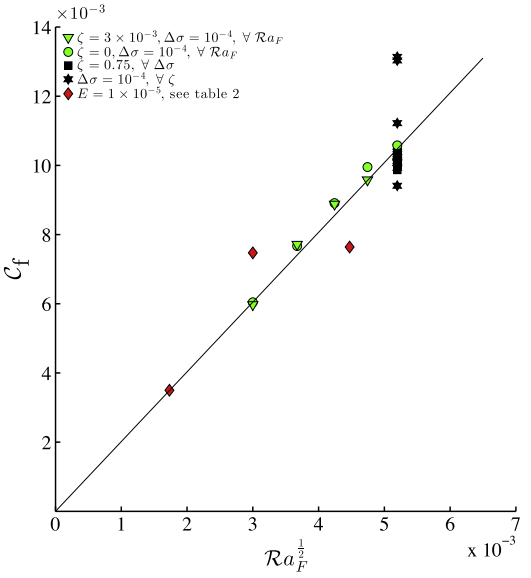

Fig. 4. Numerical verification of the thermal wind scaling for the available time-average convective shear, $\mathcal{C}_f$ (see Eq. (52) and text for details), based on 38 simulations of our suite of models (the remaining 7 are redundant and were used for benchmarking. See appendix A.1).

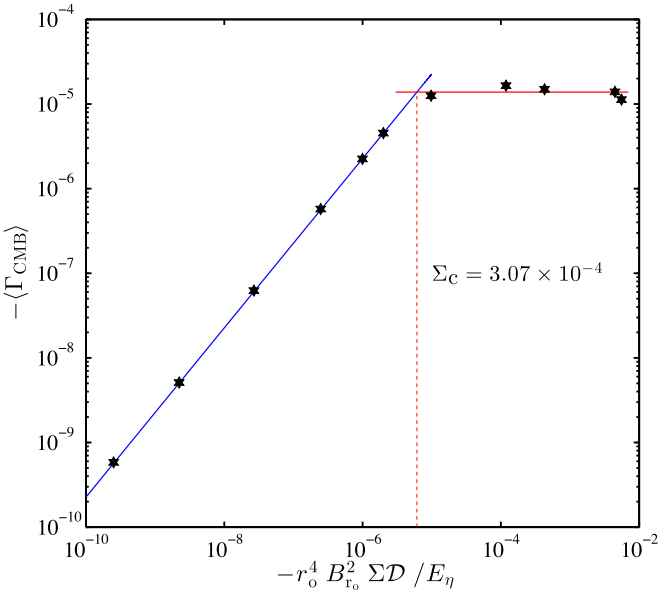

Fig. 5. Sensitivity of the opposite of the time-average electromagnetic torque of the mantle, $\langle\Gamma_{\text{CMB}}\rangle$, with respect to its control parameters r_o, $B^2_{r_o}$, Σ and $\mathcal{D}$. Same set of numerical simulations as Fig. 3a. The blue line represents a linear trend (unit slope). (For interpretation of the references to color in this figure legend, the reader is referred to the web version of this article.)

$\Sigma > \Sigma_c$, as they also reflect unrealistic geophysical situations (see section 4). Equation (36) is then further validated in Fig. 6, where we present the evolution of the electromagnetic torque exerted on the mantle for a larger subset of numerical runs verifying $\Sigma < \Sigma_c$. Based on the study of Holme (1998), the value of K_1 estimated by Dumberry (2007) was 1.3. Though our value of 2.3 is a bit higher, it is still of order one thus validating the theoretical model of Dumberry (2007).

For the electromagnetic torque at the ICB, $\langle\Gamma_{\text{ICB}}\rangle$, we seek to prove the consistency of equation (38). This scaling law involves the parameter α, representing the ratio between the local and remote contributions of the fluid on $\langle\Gamma_{\text{ICB}}\rangle$. This parameter can be

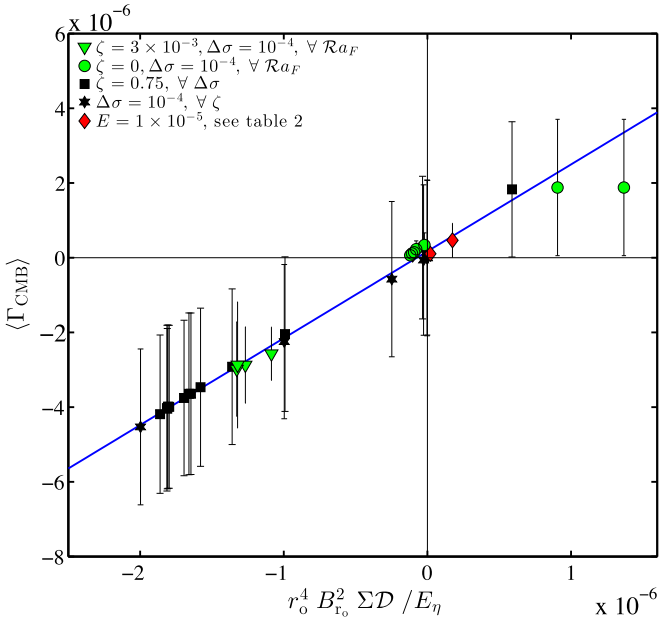

Fig. 6. Numerical verification of the scaling law for the time average electromagnetic torque at the CMB, $\langle\Gamma_{\text{CMB}}\rangle$, (see Eq. (36) and text for details) for the 33 simulations where $\Sigma < \Sigma_c$. Uncertainties as defined in Appendix A.1.

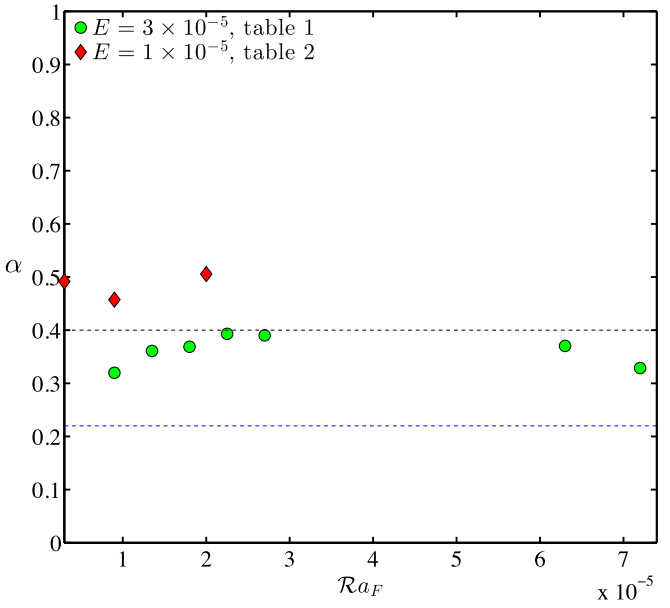

Fig. 7. Parameter dependence of the ratio α between local and remote shear influencing the time average electromagnetic torque at the ICB, $\langle\Gamma_{\text{ICB}}\rangle$, as defined in equation (38), in the 10 simulations without gravitational coupling (see Tables 1 and 2). The blue dashed-line marks the value obtained by Dumberry (2007), the black line represents the mean of our 10 numerical estimates. (For interpretation of the references to color in this figure legend, the reader is referred to the web version of this article.)

evaluated in numerical simulations where $\langle\Gamma_{\text{ICB}}\rangle$ must vanish on average, i.e. in simulations without gravitational coupling between the inner core and the mantle, $\langle\Gamma_G\rangle = 0$. In Fig. 7 we find that α is roughly constant and evolves between 0.32 and 0.55, with an average at 0.4. This is slightly higher than the value 0.22 obtained by Dumberry (2007), in an idealized configuration. Finally, in a situation where gravitational coupling is present, we have seen (Fig. 3b) that $\mathcal{C}_{\text{icb}}$ increases while α and $\mathcal{C}_f$ remain stable. This should produce a linear trend in $\langle\Gamma_{\text{ICB}}\rangle$, which we indeed observe in Fig. 8.

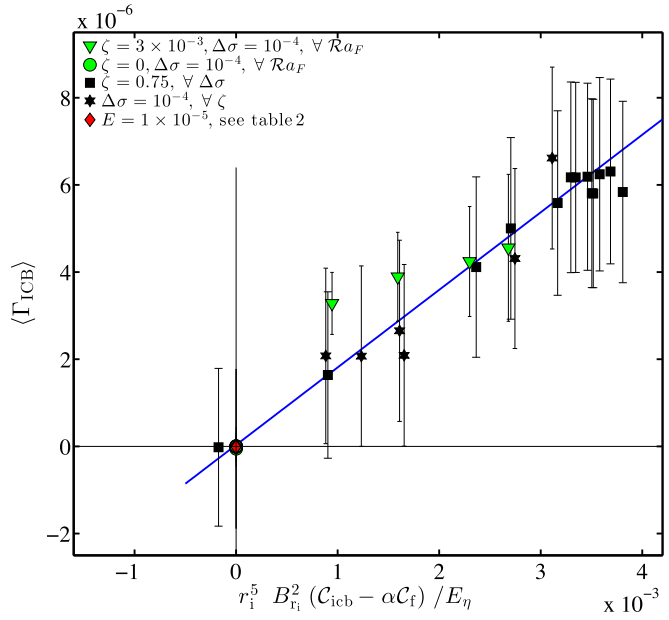

Fig. 8. Numerical verification of the scaling law for the time average electromagnetic torque at the ICB, $\langle \Gamma_{\mathrm{ICB}} \rangle$, (see Eq. (38) and text for details) for the 33 simulations where $\Sigma < \Sigma_c$. Uncertainties as defined in Appendix A.1.

Using a least-squares fitting, we obtain $K_2 = 1.1 \times 10^{-3}$, much smaller than the $\mathcal{O}(1)$ value of Dumberry (2007). We notice here the difference in behavior between a self-sustained dynamo minimizing the magnetic interactions between field and flow (Aubert, 2005), and a forced system where these interactions are maximum. This difference is best seen if we compare the poloidal magnetic field lines of an idealized model (Figs. A1 and A2 in Dumberry, 2007) with those in the tangent cylinder in Fig. 2. It is obvious that in the latter case, the field lines have adjusted to the azimuthal flow contours in order to minimize the interaction according to the Ferraro effect (Ferraro, 1937) while they are configured for a maximum interaction in the former case. This feedback, leading to a small value of K_2, could not exist in the framework of Dumberry (2007) and explains the quantitative differences in our results.

3.4. Link between $\mathcal{S}$ and $\mathcal{D}$

Fig. 9 shows the agreement of our theoretical laws (47) and (48) with numerical simulations. The contours of the predicted westward drift and inner core super-rotation are represented as functions of ϵ_1 (Eq. (44)) and ϵ_2 (Eq. (46)). We show here that the amount of shear in the fluid core which is effectively shared between $\mathcal{D}$ and $\mathcal{S}$ is $(1-\alpha)\mathcal{C}_f$. The arrows on the bottom left corners of Figs. 9a and 9b point towards the numerical simulations with no gravitational coupling ($\zeta = 0$), such that $\epsilon_1 \mapsto 0$ and $\epsilon_2 \mapsto 0$. In this situation, the whole effective shear available is located at the ICB, so that $\mathcal{S}$ is at its peak and $\mathcal{D}$ equals zero. For strong values of both the gravitational coupling and mantle conductance, $\epsilon_1 \mapsto 0$ and $\epsilon_2 \mapsto \infty$, bottom right corners, the shear is located at the ICB, but the inner core is locked to the mantle. In that case, both $\mathcal{S}$ and $\mathcal{D}$ vanish. In order to obtain a strong westward drift, the inner core must be gravitationally braked and the mantle conductance must remain bounded (top left corners in Fig. 9a, b). Finally, these figures underline two major conclusions on the behavior of the rotational dynamics of the set of coupled Earth dynamos envisaged for this study. First, as the effective shear in the fluid core is a constant, there is a clear link between the geomagnetic westward drift and the inner core super-rotation. Second, the transition between the regimes of strong $\mathcal{S}$ / vanishing $\mathcal{D}$ and strong $\mathcal{D}$ / vanishing $\mathcal{S}$ appears to be rather sharp, as it occurs over two orders of magnitude of the control parameters ϵ_1 and ϵ_2. As a consequence, a reasonable assumption is to consider that the available shear in the fluid core of the Earth is either in the inner core super-rotation or in the westward drift, but not distributed among the two. This also suggests that estimates of $\mathcal{D}$ and $\mathcal{S}$ for the Earth are likely to place tight constraints on the values of ϵ_1 and ϵ_2, and consequently on the geophysical parameters entering their definition (see the discussion below).

4. Discussion

Our suite of numerical simulations stresses the tight link between the inner core super-rotation $\mathcal{S}$ and the geomagnetic westward drift $\mathcal{D}$, as components of the long-term rotational dynamics in the Earth's core. While we rely on the theoretical approach of Dumberry (2007) to understand our results, in particular in order

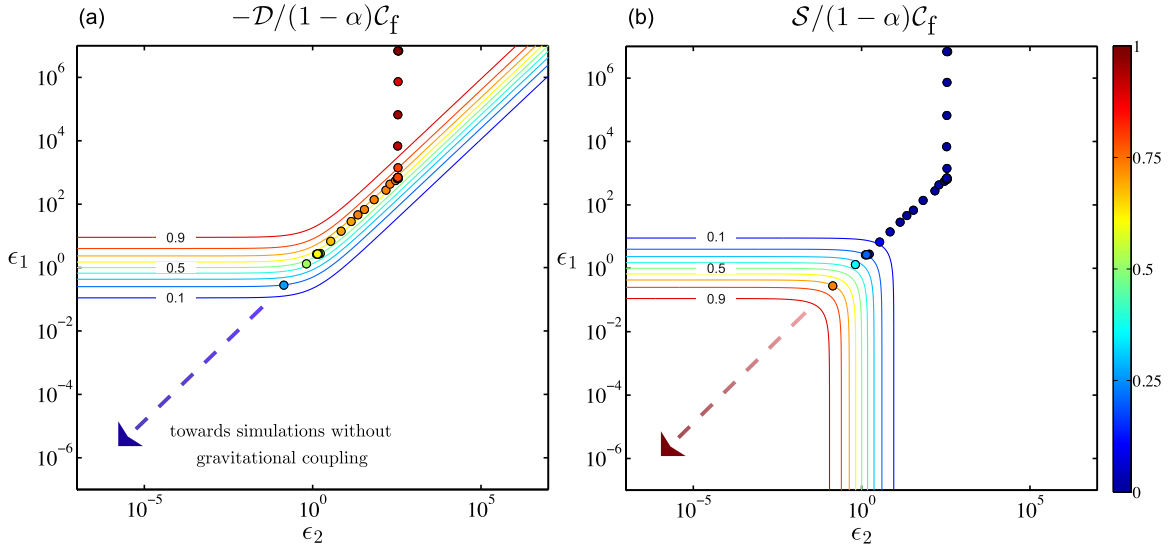

Fig. 9. Contours of the predicted westward drift $\mathcal{D}$ (a) and inner core super-rotation $\mathcal{S}$ (b) determined from equations (47) and (48). Comparison with the magnitude of $\mathcal{D}$ and $\mathcal{S}$ (colored circles) in our 27 numerical simulations with $\Sigma < \Sigma_c$ and $\mathcal{R}a_F = 2.7 \times 10^{-4}$ (see Tables 1 and 2). Arrows point towards simulations with no gravitational coupling, i.e. $\zeta = 0$. (For interpretation of the references to color in this figure legend, the reader is referred to the web version of this article.)

to analyze the long-term electromagnetic torques at work at the CMB and at the ICB, it is noteworthy that the extensive numerical study we carried out sheds new light on several aspects of the long-term rotational dynamics of the fluid outer core. First, we determined the phase diagrams for $\mathcal{S}$ and $\mathcal{D}$ (Fig. 9), together with their dependency on the convective forcing (Eq. (49)), through the convective shear $\mathcal{C}_f$ which is distributed among these two quantities. In contrast, the geomagnetic westward drift is considered as a given input in the study of Dumberry (2007). Second, the fact that the models (Eqs. (36), (38)) provide a satisfactory description of the electromagnetic torques at the fluid outer core boundaries, while only involving spherical rotation rates, needed a validation that we provide here. Finally, the very observation of the Ferraro effect diminishing the value of K_2 in equation (38) arises from a validation in self-consistent numerical simulations of the geodynamo, and could not be expected in Dumberry (2007). All these elements now give us confidence in applying our results to the Earth's core. The first quantity we wish to estimate is the convective shear $\mathcal{C}_f$ given by equation (53), which we now present in the dimensional form,

$$\mathcal{C}_f = 2.01\,\Omega\,\mathcal{R}a_F^{\frac{1}{2}}. \tag{54}$$

The flux Rayleigh number $\mathcal{R}a_F$ defined in equation (25) may also be expressed as a function of the convective dynamo power (Aubert et al., 2009) through

$$Ra_F = \frac{1}{\gamma}\frac{p}{\rho\Omega^3 D^2 V}. \tag{55}$$

Here V is the core volume and γ the conversion fraction (Eq. (18) in Aubert et al., 2009) between power p and mass anomaly flux F. We use $\rho = 11\,000\ \mathrm{kg\,m^{-3}}$ and $\Omega = 7.29\times10^{-5}\ \mathrm{rad\,s^{-1}}$ and envision a situation where the geodynamo is entirely chemically-driven, meaning a bottom-driven convection with $\gamma = 0.33$ (Aubert et al., 2009). The heat flux at the core mantle boundary Q_{CMB} is assumed to match the adiabatic value of 15 TW (Pozzo et al., 2012), so that the dynamo power is then $p = \epsilon Q_{CMB}$ with $\epsilon = 0.2$ being the combined efficiency of chemical convection and latent heat release at the ICB. This finally yields $\mathcal{R}a_F = 2.5\times10^{-12}$ and thus $\mathcal{C}_f = 0.42^\circ\ \mathrm{yr^{-1}}$. Using our mean value of $\alpha = 0.4$ (Fig. 7), we show here that the available shear distributed into $\mathcal{S}$ and $\mathcal{D}$ is then $(1-\alpha)\,\mathcal{C}_f = 0.25^\circ\ \mathrm{yr^{-1}}$. Remarkably, this is close to the mean value of the geomagnetic westward drift of $0.28^\circ\ \mathrm{yr^{-1}}$ in the Atlantic hemisphere over the last 400 yrs estimated by Finlay and Jackson (2003). This strongly suggests that a significant part, if not the whole shear available is currently in the geomagnetic westward drift, leaving the long-term inner core super-rotation close to 0, as inferred by seismological studies (see e.g. Souriau and Calvet, 2015, for a recent review of these).

In oder to have a second estimate of the proportion of the convective shear available for $\mathcal{S}$ or $\mathcal{D}$, we need to assess the values of ϵ_1 and ϵ_2 for the Earth. The dimensional form of ϵ_1 and ϵ_2 provides an overview of the geophysical parameters we have to take into account,

$$\epsilon_1 = \frac{\Gamma\tau}{K_1 B_{r_o}^2 \Delta\sigma_m r_o^4}, \tag{56}$$

$$\epsilon_2 = \frac{\Gamma\tau}{K_2 B_{r_i}^2 \sigma_c r_i^5}. \tag{57}$$

In our estimates, we use $r_i = 1220$ km, $r_o = 3480$ km, $B_{r_o} = 0.4$ mT, and the values of K_1 and K_2 found in section 3.3 ($K_1 = 2.3$, $K_2 = 1.1\times10^{-3}$). Our simulations (Tables 1 and 2) for geophysically realistic values of the mantle conductance consistently exhibit a ratio $B_{r_i}/B_{r_o} \sim 7$; so we thus set the $r.m.s$ magnetic field at the inner core boundary to $B_{r_i} = 2.8$ mT, in agreement with inferences of the magnetic field strength inside the core (Gillet et al., 2010). We also adopt the range $3\times10^{19}\ \mathrm{N\,m} < \Gamma < 2\times10^{20}\ \mathrm{N\,m}$ proposed by Davies et al. (2014) for the parameter Γ, relative to the mantle heterogeneities at the source of the gravitational torque. The core conductivity σ_c is set to $1.5\times10^6\ \mathrm{S\,m^{-1}}$ according to Pozzo et al. (2012).

The major uncertainties to assess ϵ_1 and ϵ_2 then lie in the lower mantle conductance, $\Delta\sigma_m$, and the viscous deformation time of the inner core, τ. Based on the observed out-of-phase component of the forced nutations of the Earth, Buffett (1992) inferred a lower mantle conductance of 10^8S. This value is often considered as a minimum to ensure a sufficiently strong direct electromagnetic coupling to couple the core and the mantle. Buffett (1992) proposed the existence of a thin layer at the base of the mantle, about 200 meters thick, with the same conductivity as that of the core. From a mineral physics point a view, this high conductive layer may be composed of FeO, whose conductivity was estimated as close to σ_c by Ohta et al. (2012). Another way to obtain a reasonably conducting lower mantle is to consider a thicker layer (200–300 km) of $(Mg,Fe)SiO_3$ post-perovskite, which may have an electrical conductivity greater than $10^2\ \mathrm{S\,m^{-1}}$ (Ohta et al., 2008). This would lead to a conductance larger than 2×10^7 S. The mantle conductance is also bound on the upper side by the observation of high frequencies in the core magnetic signal, constraining $\Delta\sigma_m$ to be lower than 2.5×10^9 S (Dumberry, 2007). We thus adopt a range of $2\times10^7\ \mathrm{S} < \Delta\sigma_m < 2.5\times10^9$ S. Note that this range mostly lies below the limit value $\Sigma_c\sigma_c D = 10^9$ S previously introduced in Fig. 5, meaning that our scaling laws are valid. Finally, we constrain τ using the recent mineral physics experiments of Gleason and Mao (2013) who reported an inner core viscosity range of 10^{15}–10^{18} Pa s, corresponding to $\tau = 0.02$ yr and $\tau = 20$ yr (Buffett, 1997). Considering all uncertainties on the geophysical parameters mentioned above, we obtain the following ranges of foreseeable values for ϵ_1 and ϵ_2,

$$1.4\times10^{-4} \le \epsilon_1 \le 1.1\times10^2, \tag{58}$$

$$5.4\times10^{-4} \le \epsilon_2 \le 3.6. \tag{59}$$

This indicates that our current knowledge of deep Earth physical parameters does not strongly constrain the partitioning of $(1-\alpha)\,\mathcal{C}_f$ into $\mathcal{S}$ and $\mathcal{D}$. However, for $\Delta\sigma_c$ of order 10^8 S, we may re-express our results in order to formulate a condition on the inner core viscous relaxation time for dominant westward drift. With the previously used value of the other geophysical parameters this gives $\epsilon_1 \approx \epsilon_2$, and the condition for a dominant westward drift according to Fig. 9 is then $\epsilon_1 > 1$ or $\epsilon_2 > 1$. This in turn yields $\tau > 4$ yr, meaning that the inner core must be moderately stiff, having a viscosity larger than 2×10^{17} Pa s.

Note finally that in the case $\epsilon_1 \approx \epsilon_2$, the magnitude of the shear that can be distributed into $\mathcal{S}$ and $\mathcal{D}$ is $(1-\alpha)\,\mathcal{C}_f\frac{1+\epsilon_1}{1+2\epsilon_1}$, meaning that only $(1-\alpha)\,\mathcal{C}_f/2 = 0.13^\circ\ \mathrm{yr^{-1}}$ is available if $\tau > 4$ yr (with $\epsilon_1 = \epsilon_2 \gg \mathcal{O}(1)$). The drift so available is axisymmetric. In order to match the westward drift of $0.28^\circ\ \mathrm{yr^{-1}}$ at low latitude in the Atlantic hemisphere estimated by Finlay and Jackson (2003) from historical records, an additional mechanism has to be invoked that can increase the drift rate in the Atlantic hemisphere at the expense of its Pacific counterpart. A geophysically sound possibility is that of heterogeneous buoyancy fluxes at the CMB and ICB, as advocated by Aubert et al. (2013). A hemispherical differential buoyancy release of spherical harmonic degree 1 and order 1 at the ICB can indeed generate a concentration of the drift in the Atlantic hemisphere for several centuries, leading to drift rates of about $0.23^\circ\ \mathrm{yr^{-1}}$ ($14\ \mathrm{km\,yr^{-1}}$) in this region, and a very weak drift in the Pacific hemisphere. An alternative to this mechanism is that of slow magnetic waves riding

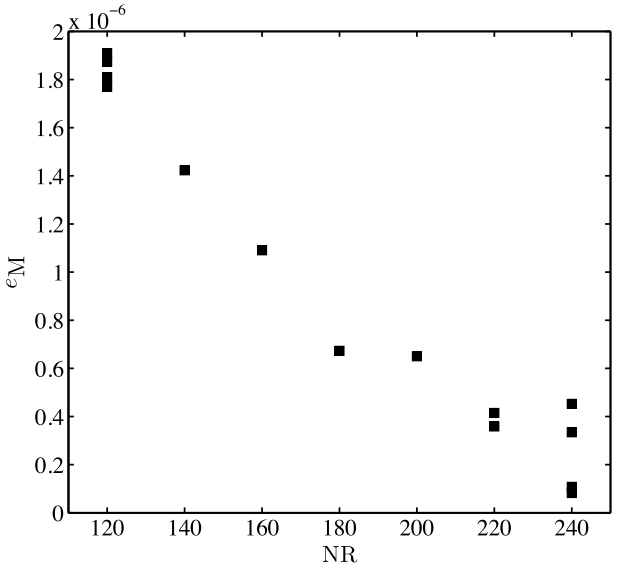

Fig. 10. Total torque balance e_M of statistically converged simulations as a function of the number of radial grid points *NR* in the fluid shell.

on top of the mean westward flow (see e.g. Hori et al., 2015). For the sake of consistency, the waves so envisioned should then be able to account for the hemispherical dichotomy of the westward drift deduced from historical records, while yielding drift rates of the order of 0.1° yr^{-1} to 0.2° yr^{-1} near the equator.

Acknowledgements

The authors would like to thank Mathieu Dumberry for discussions and comments on an early draft of the manuscript. We also thank two anonymous referees for their constructive and detailed reviews which greatly helped to improve the manuscript. JA and AF were supported by the French "Agence Nationale de la Recherche" under the grant ANR-2011-BS56-011. JA also acknowledges support from French "Programme National de Planétologie" (PNP, INSU/CNRS) in 2014. Numerical computations were performed at S-CAPAD, IPGP, France and using HPC resources from GENCI-IDRIS (Grants 2014-042122 and 2015-042122). This is IPGP contribution 3692.

Appendix A

A.1. Assessment of numerical uncertainties on torques

Each error bar pictured in Figs. 6 and 8 reflects the truncation error due to the numerical approximation of the model. In order to make our systematic analysis numerically tractable, we indeed had to use a moderate resolution (Tables 1 and 2). This error manifests itself in the long-term magnitudes of the torques. An estimate of the magnitude of this error is provided by the quantity

$$e_M = \|\langle \Gamma_{CMB} > + < \Gamma_{ICB} \rangle\|. \quad (60)$$

The error e_M should ideally vanish (Eq. (13)) and indeed converges towards 0 at a rate consistent with a second-order finite difference scheme in radius, when the radial resolution *NR* is increased (see Fig. 10).

References

Aubert, J., 2005. Steady zonal flows in spherical shell dynamos. J. Fluid Mech. (ISSN 0022-1120) 542, 53–67. http://dx.doi.org/10.1017/S0022112005006129.

Aubert, J., Aurnou, J., Wicht, J., 2008. The magnetic structure of convection-driven numerical dynamos. Geophys. J. Int. 172, 945–956. http://dx.doi.org/10.1111/j.1365-246X.2007.03693.x.

Aubert, Julien, Dumberry, Mathieu, 2011. Steady and fluctuating inner core rotation in numerical geodynamo models. Geophys. J. Int. (ISSN 0956-540X) 184 (1), 162–170. http://dx.doi.org/10.1111/j.1365-246X.2010.04842.x.

Aubert, Julien, Labrosse, Stephane, Poitou, Charles, 2009. Modelling the palaeo-evolution of the geodynamo. Geophys. J. Int. (ISSN 0956-540X) 179 (3), 1414–1428. http://dx.doi.org/10.1111/j.1365-246X.2009.04361.x.

Aubert, Julien, Finlay, Christopher C., Fournier, Alexandre, 2013. Bottom-up control of geomagnetic secular variation by the Earth's inner core. Nature (ISSN 0028-0836) 502 (7470), 219. http://dx.doi.org/10.1038/nature12574.

Aurnou, J., Brito, D., Olson, P., 1998. Anomalous rotation of the inner core and the toroidal magnetic field. J. Geophys. Res. (ISSN 2169-9313) 103 (B5), 9721–9738. http://dx.doi.org/10.1029/97JB03618.

Aurnou, J.M., Brito, D., Olson, P.L., 1996. Mechanics of inner core super-rotation. Geophys. Res. Lett. (ISSN 0094-8276) 23 (23), 3401–3404. http://dx.doi.org/10.1029/96GL03258.

Aurnou, Jonathan, Andreadis, Steven, Zhu, Lixin, Olson, Peter, 2003. Experiments on convection in earth's core tangent cylinder. Earth Planet. Sci. Lett. 212 (1), 119–134.

Braginsky, S.I., Roberts, P.H., 1995. Equations governing convection in earth's core and the geodynamo. Geophys. Astrophys. Fluid Dyn. (ISSN 0309-1929) 79 (1–4), 1–97. http://dx.doi.org/10.1080/03091929508228992.

Buffett, B.A., 1992. Constraints on magnetic energy and mantle conductivity from the forced nutations of the earth. J. Geophys. Res. (ISSN 0148-0227) 97 (B13), 19581–19597. http://dx.doi.org/10.1029/92JB00977.

Buffett, B.A., 1996. Gravitational oscillations in the length of day. Geophys. Res. Lett. (ISSN 0094-8276) 23 (17), 2279–2282. http://dx.doi.org/10.1029/96GL02083.

Buffett, B.A., 1997. Geodynamic estimates of the viscosity of the Earth's inner core. Nature (ISSN 0028-0836) 388 (6642), 571–573.

Buffett, B.A., Christensen, U.R., 2007. Magnetic and viscous coupling at the core–mantle boundary: inferences from observations of the Earth's nutations. Geophys. J. Int. (ISSN 0956-540X) 171 (1), 145–152. http://dx.doi.org/10.1111/j.1365-246X.2007.03543.x.

Buffett, B.A., Glatzmaier, G.A., 2000. Gravitational braking of inner-core rotation in geodynamo simulations. Geophys. Res. Lett. 27, 3125–3128. http://dx.doi.org/10.1029/2000GL011705.

Buffett, B.A., Mathews, P.M., Herring, T.A., 2002. Modeling of nutation and precession: effects of electromagnetic coupling. J. Geophys. Res. B (ISSN 2169-9313) 107 (B4). http://dx.doi.org/10.1029/2000JB000056.

Christensen, U.R., Aubert, J., 2006. Scaling properties of convection-driven dynamos in rotating spherical shells and application to planetary magnetic fields. Geophys. J. Int. (ISSN 0956-540X) 166 (1), 97–114. http://dx.doi.org/10.1111/j.1365-246X.2006.03009.x.

Christensen, U.R., Olson, P., 2003. Secular variation in numerical geodynamo models with lateral variations of boundary heat flow. Phys. Earth Planet. Inter. (ISSN 0031-9201) 138 (1), 39–54. http://dx.doi.org/10.1016/S0031-9201(03)00064-5.

Christensen, Ulrich R., Aubert, Julien, Hulot, Gauthier, 2010. Conditions for Earth-like geodynamo models. Earth Planet. Sci. Lett. (ISSN 0012-821X) 296 (3–4), 487–496. http://dx.doi.org/10.1016/j.epsl.2010.06.009.

Civet, F., Thebault, E., Verhoeven, O., Langlais, B., Saturnino, D., 2015. Electrical conductivity of the Earth's mantle from the first Swarm magnetic field measurements. Geophys. Res. Lett. (ISSN 0094-8276) 42 (9), 3338–3346. http://dx.doi.org/10.1002/2015GL063397.

Creager, K.C., 1997. Inner core rotation rate from small-scale heterogeneity and time-varying travel times. Science (ISSN 0036-8075) 278 (5341), 1284–1288. http://dx.doi.org/10.1126/science.278.5341.1284.

Davies, Christopher J., Stegman, D., Dumberry, M., 2014. The strength of gravitational core–mantle coupling. Geophys. Res. Lett. 41. http://dx.doi.org/10.1002/2014GL059836.

de Koker, Nico, Steinle-Neumann, Gerd, Vlček, Vojtěch, 2012. Electrical resistivity and thermal conductivity of liquid Fe alloys at high p and t, and heat flux in earth's core. Proc. Natl. Acad. Sci. 109 (11), 4070–4073. http://dx.doi.org/10.1073/pnas.1111841109.

Dormy, E., Cardin, P., Jault, D., 1998. MHD flow in a slightly differentially rotating spherical shell, with conducting inner core, in a dipolar magnetic field. Earth Planet. Sci. Lett. 160 (1–2), 15–30. http://dx.doi.org/10.1016/S0012-821X(98)00078-8.

Dumberry, M., 2007. Geodynamic constraints on the steady and time-dependent inner core axial rotation. Geophys. J. Int. (ISSN 0956-540X) 170 (2), 886–895. http://dx.doi.org/10.1111/j.1365-246X.2007.03484.x.

Eymin, C., Hulot, G., 2005. On core surface flows inferred from satellite magnetic data. Phys. Earth Planet. Inter. (ISSN 0031-9201) 152 (3), 200–220. http://dx.doi.org/10.1016/j.pepi.2005.06.009.

Ferraro, Vincent C.A., 1937. The non-uniform rotation of the sun and its magnetic field. Mon. Not. R. Astron. Soc. 97, 458–472.

Finlay, Christopher C., Jackson, A., 2003. Equatorially dominated magnetic field change at the surface of Earth's core. Science 300, 2084–2086. http://dx.doi.org/10.1126/science.1083324.

Gillet, Nicolas, Jault, Dominique, Canet, Elisabeth, Fournier, Alexandre, 2010. Fast torsional waves and strong magnetic field within the Earth's core. Nature (ISSN 0028-0836) 465 (7294), 74–77. http://dx.doi.org/10.1038/nature09010.

Glatzmaier, G.A., Roberts, P.H., 1996. Rotation and magnetism of earth's inner core. Science (ISSN 0036-8075) 274 (5294), 1887–1891. http://dx.doi.org/10.1126/science.274.5294.1887.

Gleason, A.E., Mao, W.L., 2013. Strength of iron at core pressures and evidence for a weak Earth's inner core. Nat. Geosci. (ISSN 1752-0894) 6 (7), 571–574. http://dx.doi.org/10.1038/NGEO1808.

Gomi, Hitoshi, Ohta, Kenji, Hirose, Kei, Labrosse, Stéphane, Caracas, Razvan, Verstraete, Matthieu J., Hernlund, John W., 2013. The high conductivity of iron and thermal evolution of the earth's core. Phys. Earth Planet. Inter. 224, 88–103. http://dx.doi.org/10.1016/j.pepi.2013.07.010.

Gubbins, D., 1981. Rotation of the inner core. J. Geophys. Res. (ISSN 0148-0227) 86 (NB12), 1695–1699. http://dx.doi.org/10.1029/JB086iB12p11695.

Halley, E., 1692. On the cause of the change in the variation of the magnetic needle, with a hypothesis of the structure of the internal parts of the Earth. Philos. Trans. R. Soc. Lond. 17.

Holme, R., 1998. Electromagnetic core–mantle coupling – I. Explaining decadal changes in the length of day. Geophys. J. Int. 132, 167–180. http://dx.doi.org/10.1046/j.1365-246x.1998.00424.x.

Hori, K., Jones, C.A., Teed, R.J., 2015. Slow magnetic Rossby waves in the earth's core. Geophys. Res. Lett. 42 (16), 6622–6629. http://dx.doi.org/10.1002/2015GL064733.

Jackson, A., Jonkers, A.R.T., Walker, M.R., 2000. Four centuries of geomagnetic secular variation from historical records. Philos. Trans. R. Soc. Lond. A (ISSN 1364-503X) 358 (1768), 957–990. http://dx.doi.org/10.1098/rsta.2000.0569.

Laske, G., Masters, G., 1999. Limits on differential rotation of the inner core from an analysis of the Earth's free oscillations. Nature (ISSN 0028-0836) 402 (6757), 66–69. http://dx.doi.org/10.1038/47011.

Livermore, Philip W., Hollerbach, Rainer, Jackson, Andrew, 2013. Electromagnetically driven westward drift and inner-core superrotation in earth's core. Proc. Natl. Acad. Sci. 110 (40), 15914–15918. http://dx.doi.org/10.1073/pnas.1307825110.

Murakami, M., Hirose, K., Kawamura, K., Sata, N., Ohishi, Y., 2004. Post-perovskite phase transition in $MgSiO_3$. Science (ISSN 0036-8075) 304 (5672), 855–858. http://dx.doi.org/10.1126/science.1095932.

Ohta, Kenji, Onoda, Suzue, Hirose, Kei, Sinmyo, Ryosuke, Shimizu, Katsuya, Sata, Nagayoshi, Ohishi, Yasuo, Yasuhara, Akira, 2008. The electrical conductivity of post-perovskite in Earth's D" layer. Science (ISSN 0036-8075) 320 (5872), 89–91. http://dx.doi.org/10.1126/science.1155148.

Ohta, Kenji, Cohen, R.E., Hirose, Kei, Haule, Kristjan, Shimizu, Katsuya, Ohishi, Yasuo, 2012. Experimental and theoretical evidence for pressure-induced metallization in FeO with rocksalt-type structure. Phys. Rev. Lett. (ISSN 0031-9007) 108 (2). http://dx.doi.org/10.1103/PhysRevLett.108.026403.

Olson, P., Aurnou, J., 1999. A polar vortex in the Earth's core. Nature (ISSN 0028-0836) 402 (6758), 170–173. http://dx.doi.org/10.1038/46017.

Pozzo, Monica, Davies, Chris, Gubbins, David, Alfe, Dario, 2012. Thermal and electrical conductivity of iron at Earth's core conditions. Nature (ISSN 0028-0836) 485 (7398), 355–358. http://dx.doi.org/10.1038/nature11031.

Roberts, Paul H., Aurnou, Jonathan M., 2012. On the theory of core–mantle coupling. Geophys. Astrophys. Fluid Dyn. (ISSN 0309-1929) 106 (2), 157–230. http://dx.doi.org/10.1080/03091929.2011.589028.

Roberts, P.H., Scott, S., 1965. On analysis of secular variation. 1. A hydromagnetic constraint theory. J. Geomagn. Geoelectr. (ISSN 0022-1392) 17 (2), 137–151.

Rochester, M.G., 1960. Geomagnetic westward drift and irregularities in the earth's rotation. Philos. Trans. R. Soc. Lond. A (ISSN 0080-4614) 252 (1018), 531–555. http://dx.doi.org/10.1098/rsta.1960.0014.

Rochester, M.G., 1962. Geomagnetic core–mantle coupling. J. Geophys. Res. (ISSN 0148-0227) 67 (12), 4833–4836. http://dx.doi.org/10.1029/JZ067i012p04833.

Schaeffer, Nathanaël, 2013. Efficient spherical harmonic transforms aimed at pseudospectral numerical simulations. Geochem. Geophys. Geosyst. 14 (3), 751–758. http://dx.doi.org/10.1002/ggge.20071.

Song, X.D., 2000. Joint inversion for inner core rotation, inner core anisotropy, and mantle heterogeneity. J. Geophys. Res. (ISSN 2169-9313) 105 (B4), 7931–7943. http://dx.doi.org/10.1029/1999JB900436.

Song, X.D., Richards, P.G., 1996. Seismological evidence for differential rotation of the Earth's inner core. Nature (ISSN 0028-0836) 382 (6588), 221–224. http://dx.doi.org/10.1038/382221a0.

Song, Xiaodong, Poupinet, Georges, 2007. Inner core rotation from event-pair analysis. Earth Planet. Sci. Lett. (ISSN 0012-821X) 261 (1–2), 259–266. http://dx.doi.org/10.1016/j.epsl.2007.06.034.

Souriau, A., Calvet, M., 2015. The Earth's cores. In: Dziewonski, A., Romanowicz, B. (Eds.), Treatise on Geophysics. 1.23 – Deep Earth Seismology, vol. 1, second edition. Elsevier.

Sreenivasan, Binod, Jones, Chris A., 2006. Azimuthal winds, convection and dynamo action in the polar regions of planetary cores. In: Symposium on Gedynamo-Theory, Models, Observation and Experiments. Toulouse, France, Jul. 18–20, 2005, Geophys. Astrophys. Fluid Dyn. (ISSN 0309-1929) 100 (4–5), 319–339. http://dx.doi.org/10.1080/03091920600807864.

Stewart, D.N., Busse, F.H., Whaler, K.A., Gubbins, D., 1995. Geomagnetism, earth rotation and the electrical conductivity of the lower mantle. Phys. Earth Planet. Inter. 92 (3), 199–214. http://dx.doi.org/10.1016/0031-9201(95)03035-4.

Tkalčić, Hrvoje, Young, Mallory, Bodin, Thomas, Ngo, Silvie, Sambridge, Malcolm, 2013. The shuffling rotation of the Earth's inner core revealed by earthquake doublets. Nat. Geosci. (ISSN 1752-0894) 6 (6), 497–502. http://dx.doi.org/10.1038/NGEO1813.